

## 2-1 Fluorous Nanodroplets Encapsulated within an Organopalladium Sphere

The distinctive properties of fluorous phases have practical applications in separation, purification, and reaction control in organic synthesis. In recent years, the fluorous phase has attracted much attention from the viewpoint of green chemistry. If the fluorous environment is accommodated within a nanometer-scale synthetic host, its unique fluorous properties can be available in a common aqueous or organic solvent. Here, we report the formation of a liquid-like fluorous droplet, comprised of 24 perfluoroalkyl chains confined in the interior of a 5 nanometer-sized, roughly spherical shell that spontaneously assembles in solution from 12 palladium ions and 24 bridging ligands (Fig. 1) [1].

When a mixture of ligand **1a** (11  $\mu\text{mol}$ ) and  $\text{Pd}(\text{NO}_3)_2$  (9.1  $\mu\text{mol}$ ) in dimethyl sulfoxide ( $\text{DMSO}-d_6$ ) (0.70 mL) was heated at  $70^\circ\text{C}$  for 3 hours, the endo-substituted  $\text{M}_{12}\text{L}_{24}$  complex **2a** was obtained in 100% yield, as confirmed by NMR and cold-spray ionization mass spectrometry (CSI-MS). Complexes **2b-d** were also prepared in 100% yields using the same method. We expected that the fluorous core of **2a** would be able to accommodate (or dissolve) fluorinated compounds through fluorophilic host-guest interaction. Thus, perfluorooctane (**3**), which is hardly soluble in  $\text{DMSO}$ , was mixed with a  $\text{DMSO}-d_6$  solution of **2a** (0.43 mM), and the solution was analyzed using  $^{19}\text{F}$  NMR. We observed four signals from **3** in addition to the six signals from **2a**. On average, 5.8 molecules of the guest **3** were accommodated by the capsule **2a**. This host-guest ratio remained almost unchanged even if the experiment was carried out at different concentrations ( $[\mathbf{2a}] = 0.18, 0.37, \text{ or } 0.54 \text{ mM}$ ). The accommodation was controllable by varying the lengths of fluorinated sidechains.

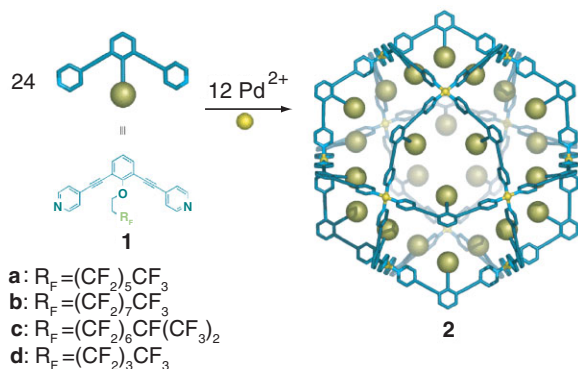


Figure 1 Schematic presentation for the self-assembly of endo-fluorous  $\text{M}_{12}\text{L}_{24}$  molecular spheres.

The complex **2a** possesses a “raw egg” structure with a rigid spherical  $\text{M}_{12}\text{L}_{24}$  shell framework and flexible perfluoroalkyl chains that probably behave like a liquid within the shell. A crystallographic analysis confirmed this structure (Fig. 2). For this analysis we obtained a single crystal of a  $\mathbf{2a}\cdot(\mathbf{3})_n$  complex, and analyzed the crystal using X-ray crystallography. Whereas the spatial resolution afforded by a conventional laboratory diffractometer was insufficient to determine the structure, use of the synchrotron X-ray radiation at AR-NW2 allowed us to obtain impressive high-quality data from which the  $\text{M}_{12}\text{L}_{24}$  shell framework of **2a** was refined. Although it was possible to refine the rigid shell framework of **2a**, the fluorous sidechains and guest molecules were completely disordered and could not be located. This indicates that the interior sidechains are flexible enough that we can consider the core as a liquid-like nanospace.

We have demonstrated the construction of a nano-fluorous droplet in an organic solvent exploiting the efficient self-assembly of ligands and transition metals. The central cavity is large and can effectively uptake up to eight fluorocarbon molecules. The ability of encapsulation could be precisely controlled by the design of perfluoroalkyl groups. The high degree of variety and precision in designing and synthesizing organic ligand molecules promises further applications.

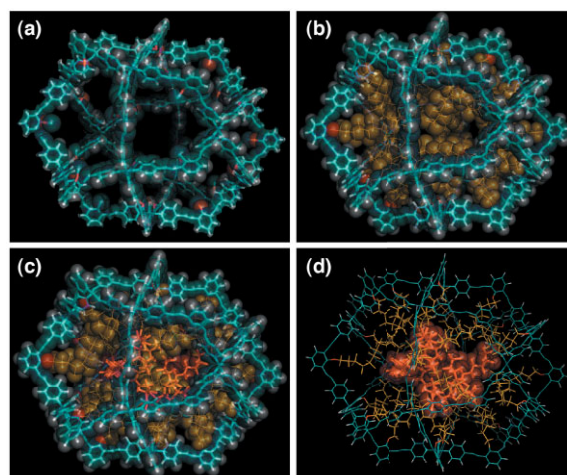


Figure 2 The molecular structure of **2a**. (a) The structure of the shell framework of **2a** as determined using X-ray crystallography. The  $\text{C}_6\text{F}_{13}\text{CH}_2$ - side chains at the curvature of the ligands are disordered and could not be located. (b) Including a model of the  $\text{C}_6\text{F}_{13}(\text{CH}_2)_2$ - side chains, with only the chains optimized using a force-field calculation. Six molecules of perfluorooctane are placed within the central void of **2a** (c), and a molecular dynamics simulation of structural annealing from 2000 K to 300 K are carried out (d).

S. Sato<sup>1,2</sup>, J. Iida<sup>1,2</sup>, K. Suzuki<sup>1,2</sup>, M. Kawano<sup>1,2</sup>, T. Ozeki<sup>3</sup> and M. Fujita<sup>1,2</sup> (<sup>1</sup>The Univ. of Tokyo, <sup>2</sup>JST-CREST, <sup>3</sup>Tokyo Inst. of Tech.)

## Reference

- [1] S. Sato, J. Iida, K. Suzuki, M. Kawano, T. Ozeki, M. Fujita, *Science*, **313** (2006) 1273.

## 2-2 X-Ray Absorption Fine Structure (XAFS) Study of Rh-Cr Mixed-Oxide Cocatalyst Dispersed on Visible-Light-Driven $(\text{Ga}_{1-x}\text{Zn}_x)(\text{N}_{1-x}\text{O}_x)$ Photocatalysts

It is well-known that cocatalysts loaded on photocatalysts enhance photocatalytic activities. In the case of overall water splitting, the cocatalysts such as  $\text{NiO}_x$  [1] and  $\text{RuO}_2$  [2] assist in  $\text{H}_2$  and  $\text{O}_2$  evolution. We have previously reported [3-6] that the solid solution of GaN and ZnO,  $(\text{Ga}_{1-x}\text{Zn}_x)(\text{N}_{1-x}\text{O}_x)$ , becomes an active and stable photocatalyst for overall water splitting under visible-light irradiation when loaded with  $\text{RuO}_2$  nanoparticles. Recently, we found that the dispersion of Rh-Cr mixed-oxide nanoparticles on  $(\text{Ga}_{1-x}\text{Zn}_x)(\text{N}_{1-x}\text{O}_x)$  results in a comparatively effective catalyst for  $\text{H}_2$  evolution, achieving a quantum efficiency of ca. 2.5% under irradiation at 420-440 nm. This is the highest value reported for photocatalytic overall water splitting under visible-light irradiation [7]. In the current study, the structures of the Rh-Cr mixed-oxide cocatalysts on  $(\text{Ga}_{1-x}\text{Zn}_x)(\text{N}_{1-x}\text{O}_x)$  were characterized using X-ray absorption spectroscopy (XAS) to clarify the relationship between the structure of the cocatalyst and the photocatalytic activity for overall water splitting [8, 9].

The  $(\text{Ga}_{1-x}\text{Zn}_x)(\text{N}_{1-x}\text{O}_x)$  solid solution was prepared at 1123 K using a  $\text{Ga}_2\text{O}_3$  and ZnO mixture. Rh-Cr mixed oxide cocatalysts were loaded onto the catalysts by impregnation from an aqueous solution containing  $\text{Na}_3\text{RhCl}_6 \cdot 2\text{H}_2\text{O}$  and  $\text{Cr}(\text{NO}_3)_3 \cdot 9\text{H}_2\text{O}$ , followed by calcination at various temperatures in air. XAFS measurements at the Cr-K and Rh-K edges carried out at BL-12C of the PF and BL01B1 of the SPring-8, respectively. The absorption spectra were recorded in either the transmission or fluorescence mode at room temperature and ambient pressure using a Si(111) double-crystal monochromator, and data reduction was performed using the REX2000 program (Rigaku Corporation). The Fourier transforms of the  $k^3$ -weighted extended X-ray absorption fine structure (EXAFS) spectra were typically in the 3.0-12.0  $\text{\AA}^{-1}$  region.

Figure 3 shows the Rh-K and Cr-K edge X-ray absorption near edge structure (XANES) spectra for 1 wt% Rh - 1.5 wt% Cr/ $(\text{Ga}_{1-x}\text{Zn}_x)(\text{N}_{1-x}\text{O}_x)$  calcinated at various temperatures (c-f), compared to  $\text{Na}_3\text{RhCl}_6 \cdot 2\text{H}_2\text{O}$ ,  $\text{Cr}(\text{NO}_3)_3 \cdot 9\text{H}_2\text{O}$ , and  $\text{Rh}_{0.5}\text{Cr}_{1.5}\text{O}_3$  reference spectra (a,g). The Rh-K edge XANES spectrum for the impreg-

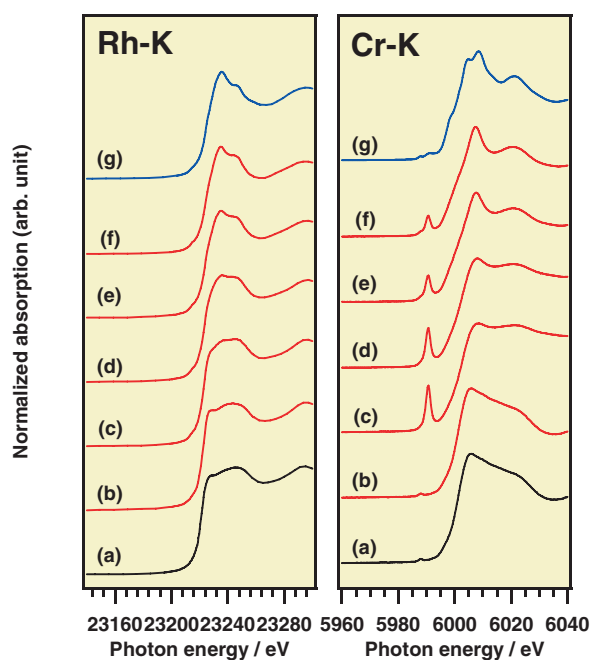


Figure 3 Rh-K and Cr-K edge XANES spectra. (a)  $\text{Na}_3\text{RhCl}_6 \cdot 2\text{H}_2\text{O}$  (Rh-K edge) or  $\text{Cr}(\text{NO}_3)_3 \cdot 9\text{H}_2\text{O}$  (Cr-K edge) reference spectra. (b)  $(\text{Ga}_{1-x}\text{Zn}_x)(\text{N}_{1-x}\text{O}_x)$  loaded with 1 wt% Rh and 1.5 wt% Cr after impregnation, and followed by calcination at (c) 523, (d) 573, (e) 623, and (f) 673 K. (g)  $\text{Rh}_{0.5}\text{Cr}_{1.5}\text{O}_3$ .

nated sample (b) clearly differs from that of  $\text{Rh}_{0.5}\text{Cr}_{1.5}\text{O}_3$  (g) but is very similar to that of  $\text{Na}_3\text{RhCl}_6 \cdot 2\text{H}_2\text{O}$  (a). The spectra show a change at 523 K (c), and become similar to the spectra for the  $\text{Rh}_{0.5}\text{Cr}_{1.5}\text{O}_3$  reference above 623 K, indicating that the  $\text{Na}_3\text{RhCl}_6 \cdot 2\text{H}_2\text{O}$  precursor on the  $(\text{Ga}_{1-x}\text{Zn}_x)(\text{N}_{1-x}\text{O}_x)$  surface decomposes and converts to trivalent Rh-Cr mixed oxide at elevated calcination temperature. The Cr-K edge XANES spectra also change remarkably with increasing calcination temperature. The pre-edge peak, which is assigned to  $\text{Cr}^{6+}$ , becomes weaker with increasing calcination temperature, and the spectrum becomes similar to that for  $\text{Rh}_{0.5}\text{Cr}_{1.5}\text{O}_3$ . The same behavior is also observed in the Fourier transforms of the  $k^3$ -weighted EXAFS spectra, which are shown in Fig. 4. The peak assigned to the Rh-Cl shell appears in the spectra of both the sample after impregnation and of samples calcinated at temperatures of up to 573 K. However, this peak weakens with increasing calcination temperature, and is undetectable at 673 K. The Rh-(O)-Rh or Cr peak also becomes stronger with increasing calcination temperature.

In summary, we have investigated the formation and structural characteristics of Rh and Cr species dispersed on  $(\text{Ga}_{1-x}\text{Zn}_x)(\text{N}_{1-x}\text{O}_x)$  as cocatalysts for photocatalytic overall water splitting. With increasing calcination temperature, the  $\text{Na}_3\text{RhCl}_6 \cdot 2\text{H}_2\text{O}$  precursor on the  $(\text{Ga}_{1-x}\text{Zn}_x)(\text{N}_{1-x}\text{O}_x)$  surface decomposes and converts to trivalent Rh-Cr mixed-oxide at 623 K, resulting in an increase in activity for the water splitting reaction, with maximum activity at 1 wt% Rh and 1.5 wt% Cr.

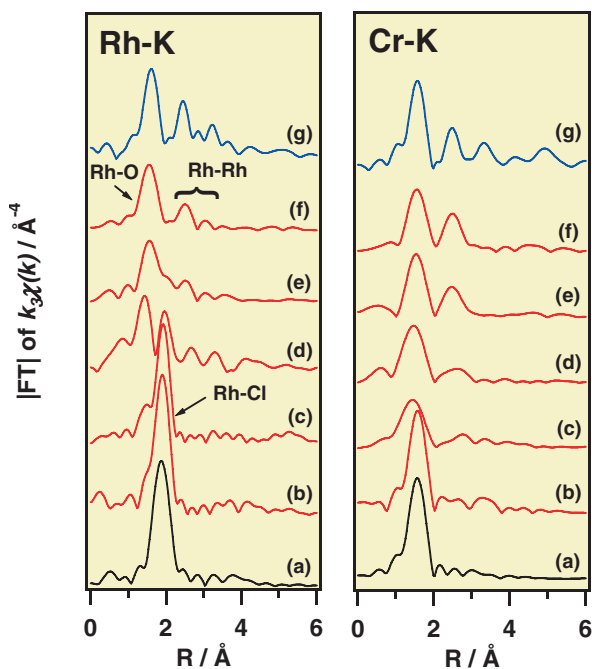


Figure 4  
Fourier transforms of the  $k^2$ -weighted Rh-K and Cr-K edge EXAFS spectra shown in Fig. 3. (a)  $\text{Na}_3\text{RhCl}_6 \cdot 2\text{H}_2\text{O}$  (Rh-K edge) or  $\text{Cr}(\text{NO}_3)_3 \cdot 9\text{H}_2\text{O}$  (Cr-K edge) reference spectra. (b)  $(\text{Ga}_{1-x}\text{Zn}_x)(\text{N}_{1-x}\text{O}_x)$  loaded with 1 wt% Rh and 1.5 wt% Cr after impregnation, and followed by calcination at (c) 523, (d) 573, (e) 623, and (f) 673 K. (g)  $\text{Rh}_{0.5}\text{Cr}_{1.5}\text{O}_3$ .

**K. Teramura, K. Maeda, N. Saito, Y. Inoue and K. Domen (The Univ. of Tokyo)**

#### References

- [1] K. Domen, S. Naito, M. Soma, T. Onishi and K. Tamaru, *J. Chem. Soc., Chem. Commun.*, (1980) **543**.
- [2] Y. Inoue, T. Niiyama, Y. Asai and K. Sato, *J. Chem. Soc., Chem. Commun.*, (1992) **579**.
- [3] K. Maeda, T. Takata, M. Hara, N. Saito, Y. Inoue, H. Kobayashi and K. Domen, *J. Am. Chem. Soc.*, **127** (2005) 8286.
- [4] K. Maeda, K. Teramura, T. Takata, M. Hara, N. Saito, K. Toda, Y. Inoue, H. Kobayashi and K. Domen, *J. Phys. Chem. B*, **109** (2005) 20504.
- [5] K. Teramura, K. Maeda, T. Saito, T. Takata, N. Saito, Y. Inoue and K. Domen, *J. Phys. Chem. B*, **109** (2005) 21915.
- [6] K. Teramura, K. Maeda, T. Saito, T. Takata, N. Saito, Y. Inoue and K. Domen, *J. Phys. Chem. B*, **110** (2006) 4500.
- [7] K. Maeda, K. Teramura, D. Lu, T. Takata, N. Saito, Y. Inoue and K. Domen, *Nature*, **440** (2006) 295.
- [8] K. Maeda, K. Teramura, H. Masuda, T. Takata, N. Saito, Y. Inoue and K. Domen, *J. Phys. Chem. B*, **110** (2006) 13107.
- [9] K. Maeda, K. Teramura, D. Lu, T. Takata, N. Saito, Y. Inoue and K. Domen, *J. Phys. Chem. B*, **110** (2006) 13753.

## 2-3 Sulfur K-Edge Extended X-Ray Absorption Fine Structure (EXAFS) Analysis of Group 12 Metal(II) Complexes

Little attention has hitherto been paid to the physico-chemical properties of small molecule complexes with Group 12 metal(II) ions, since these metals have filled  $d^{10}$  electronic configurations and their ligand complexes are usually stabilized by aromatic rings or multiple

bonds. The Group 12 metals, however, are one of the essential metals, and perform vitally important roles in biological systems. In many enzymes, metal(II)-sulfur bonds are prevalent, and thus the structures and properties of thiolato complexes with metal(II) have been investigated as model compounds. Our basic strategy is to use spectroscopic methods to study Group 12 metal(II) thiolato complexes which have “saturated” simple supporting ligands, in order to identify their coordination atoms and structural geometry [1, 2]. For Zn(II) and Cd(II) complexes, metal K-edge X-ray absorption near edge structure (XANES) spectroscopy cannot be used to directly determine the site symmetry and electronic state [3]. On the other hand, extended X-ray absorption fine structure (EXAFS) studies can provide detailed information. The sulfur K-edge energy is relatively low (2471 eV) compared with those of the metals. However, the sulfur K-edge EXAFS method can provide direct information on the sulfur atom environment, which cannot be obtained from the complementary metal K-edge measurements. We report here sulfur K-edge EXAFS spectroscopy studies on Zn(II) and Cd(II) complexes such as  $(\text{Et}_4\text{N})[\text{Zn}(\text{SAd})_3]$  (1),  $(\text{Et}_4\text{N})_2[\{\text{Zn}(\text{ScHex})_2\}_2(\mu\text{-ScHex})_2]$  (2), and  $(\text{Et}_4\text{N})_2[\{\text{Cd}(\text{ScHex})\}_4(\mu\text{-ScHex})_6]$  (3), where HSA represents 1-adamantanethiol and HS-ScHex does cyclohexanethiol. The structures of 1 and 2 represent typical examples, and adamantane type clusters of 3 are sometimes observed in Group 12 metal(II) complexes [4].

The molecular structures determined using X-ray diffraction of complexes 1-3 [2, 4] are shown in Fig. 5. Complex 1 has a mononuclear  $\text{ZnS}_3$  plane with average bond lengths of Zn-S: 2.262(4), S...S: 3.917(4), S-C: 1.844(9), S...C<sub>far</sub>: 2.770(9) Å. Complex 2 has a dinuclear structure containing two  $\text{ZnS}_3$  units bridged by two sulfur atoms (average bond lengths of Zn-S: 2.352(1), S...S: 3.864(2), S-C: 1.831(5), S...C<sub>far</sub>: 2.779(5) Å). The atoms defined as C<sub>far</sub> are the carbon atoms next to the carbon atoms which directly bond to the sulfur atom (see the bold dashed blue lines in Fig. 5). In complex 3, four Cd(II) ions and six sulfur atoms form a  $\text{Cd}_4\text{S}_6$  adamantane-like cage. Each Cd(II) ion forms a tetrahedral configuration, with one terminal ( $\text{S}_t$ ) and three bridging ( $\text{S}_b$ ) ligands (average bond lengths of Cd-S<sub>t</sub>: 2.485(2)-2.502(3) Å, Cd-S<sub>b</sub>: 2.542(2)-2.576(3) Å,  $\text{S}_b\cdots\text{S}_b$ : 3.896(3)-4.355(3) Å,  $\text{S}_b\cdots\text{S}_t$ : 4.052(4)-4.349(4) Å).

The sulfur K-edge EXAFS studies of complexes 1-3 were carried out at BL-9A, and Fourier transforms of the spectra are shown in Fig. 6 along with corresponding spectral fits. The EXAFS results are in good agreement with the crystallographic data. It is worth noticing that S...S interactions were observed clearly in all the spectra. The S...S bond length in complex 1 (3.914 Å) is longer than that in complex 2 (3.827 Å). This trend is due to the structural difference of the Zn(II) ion, which is planar in complex 1 and tetrahedral in complex 2. In complex 3, the S...S distances vary widely from 3.896(3) Å to 4.355(3) Å. The accuracy of the EXAFS data fitting

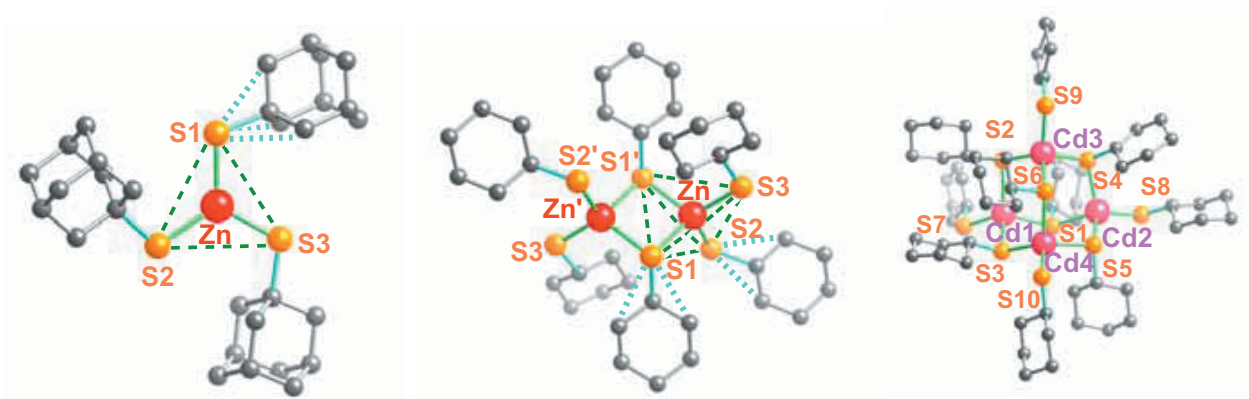


Figure 5  
Molecular Structures of  $[\text{Zn}(\text{SAd})_3]^-$  (1),  $[\{\text{Zn}(\text{ScHex})_2\}_2(\mu\text{-ScHex})_2]^{2-}$  ( $2^{2-}$ ), and  $[\{\text{Cd}(\text{ScHex})_4(\mu\text{-ScHex})_6\}]^{3-}$  ( $3^{2-}$ ). The solid green line represents the M-S bond, the blue line S-C, the dashed green line S...S, and the bold dashed blue line S...C<sub>far</sub>. For clarity, some lines are omitted.

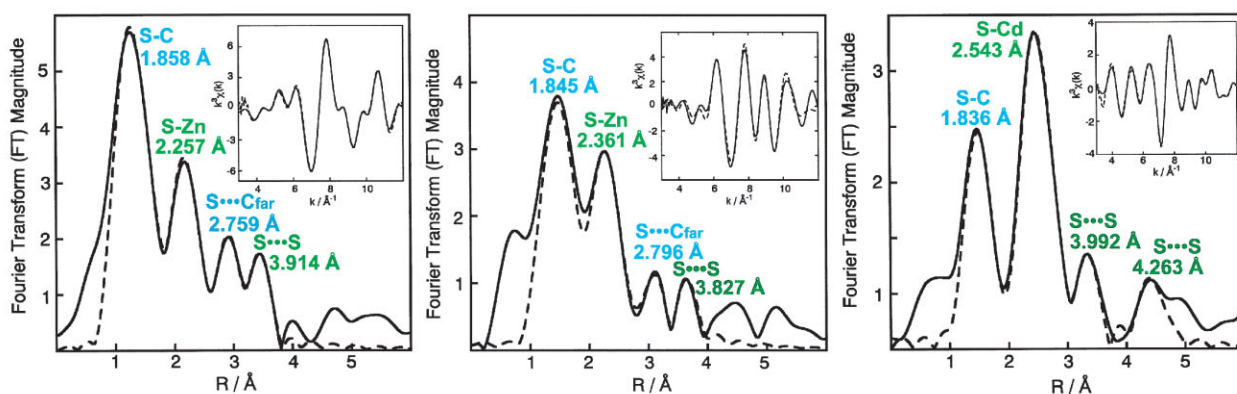


Figure 6  
Sulfur K-edge EXAFS Fourier transforms for complexes 1 (left), 2 (center), and 3 (right). The solid line represents the experimental data and the dashed line a fit to the data. (Inset: the  $k^3$ -weighted sulfur K-edge EXAFS spectrum of each complex (solid lines), along with a fit to the data (dashed lines)).

improves when the S...S interactions are divided into two parts, with short S...S interactions (3.992 Å) and longer ones (4.263 Å). In addition, S...C<sub>far</sub> interactions of 2.759 Å for complex 1 and 2.796 Å for complex 2 also contribute to these results.

In summary, both S...S and S...C<sub>far</sub> interactions have been clearly detected. The new methodology of sulfur K-edge EXAFS spectroscopy could be further applied to the structural determination of metalloproteins and small molecule complexes.

**K. Fujisawa, Y. Miyashita and K. Okamoto (Univ. of Tsukuba)**

#### References

- [1] Y. Matsunaga, K. Fujisawa, N. Amir, Y. Miyashita and K. Okamoto, *Appl. Organomet. Chem.*, **19** (2005) 778.
- [2] Y. Matsunaga, K. Fujisawa, N. Ibi, N. Amir, Y. Miyashita and K. Okamoto, *Bull. Chem. Soc. Jpn.*, **78** (2005) 1285.
- [3] J. E. Penner-Hahn, *Coord. Chem. Rev.*, **249** (2005) 161.
- [4] Y. Matsunaga, K. Fujisawa, N. Ibi, M. Fujita, T. Ohashi, N. Amir, Y. Miyashita, K. Aika, Y. Izumi and K. Okamoto, *J. Inorg. Biochem.*, **100** (2006) 239.

## 2-4 Mercury(II) Cysteine Complexes in Alkaline Aqueous Solution

Inorganic mercury toxicity has been proposed to result from the high affinity of Hg(II) to cysteine-containing biomolecules, leading to damaged enzymes and disruption in membrane transport *in vivo*. To investigate the nature of the interaction, we studied the structure and speciation of Hg(II) complexes in aqueous solutions with the amino acid L-cysteine ( $\text{H}_2\text{Cys}$ ).

Five solutions with  $[\text{Hg}^{2+}] \sim 90$  mmol/L and  $\text{H}_2\text{Cys}/\text{Hg}(\text{II})$  molar ratios of 2.2 (A), 3.3 (B), 4.3 (C), 5.3 (D), and 10.1 (E) were prepared at pH = 11 under inert atmosphere. Hg L<sub>III</sub>-edge extended X-ray absorption fine structure (EXAFS) spectra were collected at BL-10B. Analyses of the EXAFS spectra for solutions A - E by least-squares curve fitting revealed that the Hg-S coordination number (C.N.) varied from 2.1 (A) to 3.5 (E), and the mean Hg-S bond distances from 2.36 Å (A), 2.39

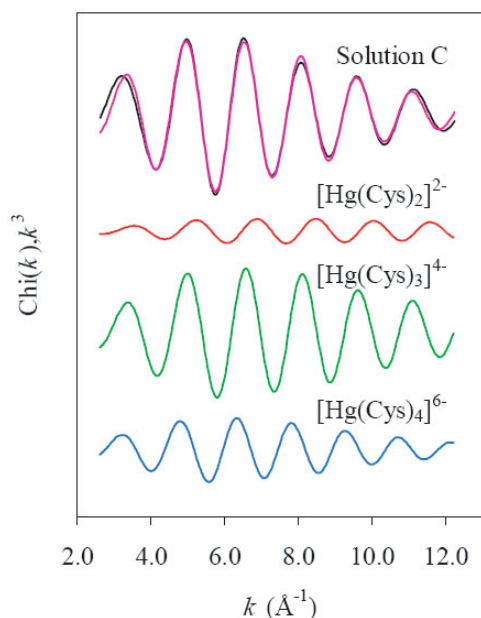


**Figure 7**  
Hg L<sub>III</sub>-edge  $k^2$ -EXAFS oscillation of solution C fitted to a linear combination of Hg-S interactions for  $\text{Hg}(\text{Cys})_2$  (12%),  $\text{Hg}(\text{Cys})_3$  (62%) and  $\text{Hg}(\text{Cys})_4$  (26%).

Å (**B**), 2.44 Å (**C**), 2.50 Å (**D**) to 2.50 Å (**E**), with an accuracy of 20% in the C.N. and  $\pm 0.02$  Å for the distance. A literature survey of Hg(II)-thiolate (SR) crystals showed a direct correlation between the number of coordinated ligands and the average Hg-S bond distance for linear  $[\text{Hg}(\text{SR})_2]$  (2.32 – 2.36 Å), trigonal  $[\text{Hg}(\text{SR})_3]$  (2.42 – 2.44 Å) and distorted tetrahedral  $[\text{Hg}(\text{SR})_4]^{2-}$  (2.52 – 2.54 Å) complexes.

The amount of the  $[\text{Hg}(\text{Cys})_2]^{2-}$  complex was evaluated by integrating the calibrated S-Hg-S stretching vibrational Raman band of the complex. The formation of higher complexes was monitored by  $^{199}\text{Hg}$  NMR spectroscopy.

The distribution of the  $[\text{Hg}(\text{Cys})_n]^{2-2n}$  ( $n = 2, 3, 4$ ) species was obtained by fitting linear combinations of simulated EXAFS oscillations for each complex, which were generated theoretically by means of FEFF 8.1 program [1], to the Fourier-filtered EXAFS oscillation for each solution (Fig. 7, Table 1). The best fits were obtained by assuming average Hg-S distances of 2.35(2), 2.44(2) and 2.52(2) Å for the  $\text{Hg}(\text{Cys})_2$ ,  $\text{Hg}(\text{Cys})_3$  and  $\text{Hg}(\text{Cys})_4$  species, respectively, and the corresponding Debye-Waller parameters  $\sigma^2 = 0.003, 0.006$  and  $0.008$  Å<sup>2</sup>, calculated by the FEFF 8.1 program [1].

The combined results showed that solutions **A**,

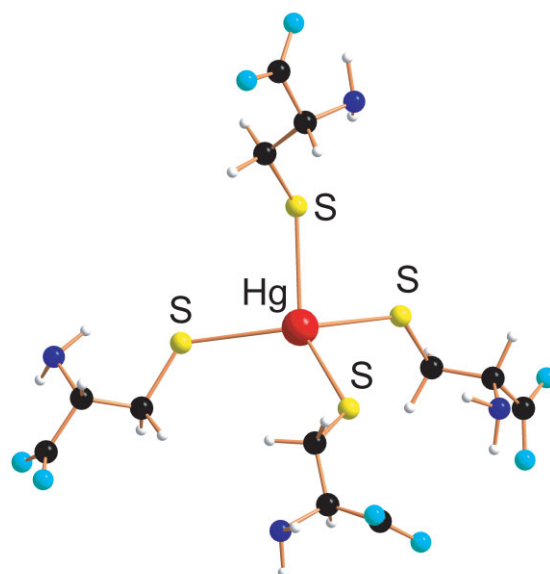


**Figure 8**  
The structure of the novel complex  $[\text{Hg}(\text{Cys})_4]^{6-}$  as obtained from theoretical optimization, consistent with EXAFS and  $^{199}\text{Hg}$  NMR results for alkaline solutions with large cysteine excess and  $[\text{Hg}^{II}] \sim 0.09$  M [2].

and **C** are dominated by  $[\text{Hg}(\text{Cys})_2]^{2-}$  and  $[\text{Hg}(\text{Cys})_3]^{4-}$  species, respectively. The Hg-S distance 2.50(2) Å for solutions **D** and **E** reveals a novel four-coordinated  $[\text{Hg}(\text{Cys})_4]^{6-}$  complex (Fig. 8), supported by the  $^{199}\text{Hg}$  NMR chemical shift. For intermediate ligand to metal ratios, the mean Hg-S bond distance indicates a mixture of three  $[\text{Hg}(\text{Cys})_n]^{2-2n}$  ( $n = 2, 3, 4$ ) species, consistent with a principal component analysis of the EXAFS spectra.

In summary, we could structurally characterize Hg(II) complexes with L-cysteine in alkaline aqueous solutions by means of EXAFS spectroscopy. The distribution of the  $[\text{Hg}(\text{Cys})_n]^{2-2n}$  ( $n = 2, 3$  and  $4$ ) species in mercury(II) solutions with different  $\text{H}_2\text{Cys} / \text{Hg}^{II}$  ratios has been evaluated by deconvolution of EXAFS spectra, aided by principal component analysis,  $^{199}\text{Hg}$  NMR and Raman results. The novel four-coordinated  $[\text{Hg}(\text{Cys})_4]^{6-}$  species dominates in solutions with large excess of cysteine.

## B. O. Leung and F. Jalilehvand (Univ. of Calgary)

### References

- [1] A. L. Ankudinov and J. J. Rehr, *Phys. Rev. B* **56**, (1997) R1712.
- [2] F. Jalilehvand, B. O. Leung, M. Izadifard and E. Damian, *Inorg. Chem.*, **45** (2006) 66.

**Table 1** Relative amount (%) of  $\text{Hg}(\text{Cys})_n$  species in solutions A – E from EXAFS, Raman and  $^{199}\text{Hg}$  NMR.

Solution	$\text{H}_2\text{Cys}/\text{Hg}(\text{II})$	$\text{Hg}(\text{Cys})_2$	$\text{Hg}(\text{Cys})_3$	$\text{Hg}(\text{Cys})_4$
<b>A</b>	2.2	94	6	
<b>B</b>	3.3	42	58	
<b>C</b>	4.3	12	62	26
<b>D</b>	5.3	5	22	73
<b>E</b>	10.1		~15	~85

## 2-5 Dynamical Valence Fluctuations in $[\text{Pt}(\text{chxn})_2\text{I}]_2$ (chxn: 1R, 2R-Diaminocyclohexane) Observed Using X-Ray Diffuse Scattering, ESR and STM Techniques

One-dimensional (1D) electron systems are of much interest in the field of solid-state chemistry and physics, because of their pronounced characteristic phenomena. Halogen-bridged 1D metal complexes (MX-chains) have also become attractive targets of study as model compounds of the 1D Peierls-Hubbard type, since they have a variety of electronic states which can be tuned by substitution of their components. MX-chain complexes with a mixed-valence structure  $-\text{X}\cdots\text{M}^{2+}\cdots\text{X}-\text{M}^{4+}-\text{X}\cdots$  (where  $\text{M} = \text{Pd}, \text{Pt}$  and  $\text{X} = \text{Cl}, \text{Br}, \text{I}$ ) have been widely studied as 1D materials with strong electron-lattice interactions. Their Peierls distorted 1D structure is noted as having a charge-density-wave (CDW) state, and unique optical and dynamical properties have been reported.

The CDW compounds have been classified into two categories depending on the strength of the inter-chain interaction, namely, 1D-CDW and 2D-CDW (schematically illustrated in Figs. 9a and 9b). In the 1D-CDW compounds, the CDW phase has no correlation between the neighboring chains. In the 2D-CDW compounds, hydrogen bonds between the 1D chains induce short range ordering, with 2D sheets of a same phase. This structure should therefore be referred to as “quasi-2D-CDW”. In quasi-2D-CDWs, although a CDW phase boundary must exist (Fig. 9c), the electronic structure of such boundaries has not yet been well understood. In this study, we have determined that the electronic structure at the CDW boundary region of an iodo-bridged Pt compound  $[\text{Pt}(\text{chxn})_2\text{I}]_2$  has a quasi-2D-CDW ground state. The study made use of X-ray diffuse scattering, scanning tunneling microscopy (STM), and electron spin resonance (ESR) methods, which are sensitive to three distinct timescales [1].

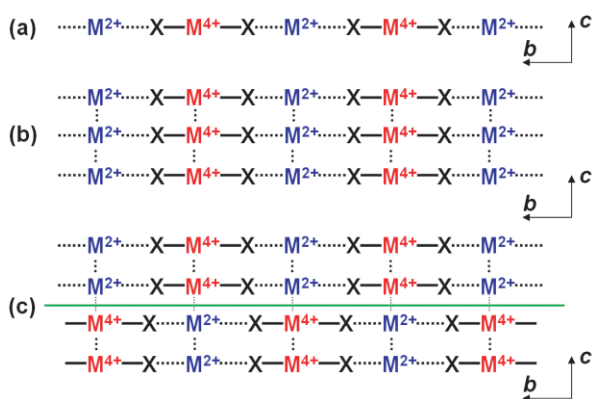


Figure 9 Schematic valence arrangement in halogen-bridged CDW compounds. (a) 1D-CDW, (b) 2D-CDW, (c) CDW phase boundary (green line) in quasi-2D-CDW.

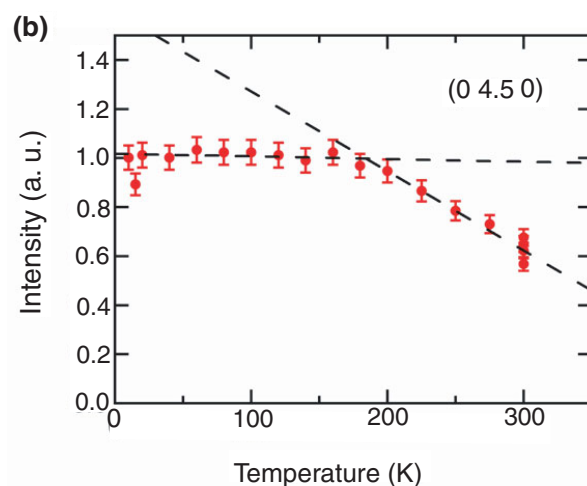
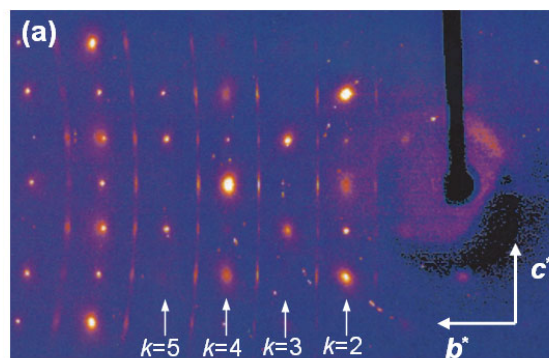


Figure 10 a) Oscillation photograph of  $[\text{Pt}(\text{chxn})_2\text{I}]_2$  on the  $b^*c^*$  plane. b) Normalized X-ray diffuse scattering intensity of  $[\text{Pt}(\text{chxn})_2\text{I}]_2$  at  $(0\ 4.5\ 0)$  as a function of temperature.

Figure 10a shows an oscillation photograph of  $[\text{Pt}(\text{chxn})_2\text{I}]_2$  recorded at BL-1B. The intensity distribution in the  $c^*$ -direction peaks at integer values of  $\zeta$  with a FWHM of approximately 0.25 reciprocal lattice units, indicating that the CDW phase has short range order (quasi-2D-CDWs) along the  $c$ -axis. Figure 10b shows the temperature dependence of the X-ray diffuse scattering intensity at  $(0\ 4.5\ 0)$  measured at BL-4C. Below 180 K, the intensity is almost temperature independent, whereas a decrease in intensity of about 30% is seen upon increasing the temperature from 180 K to 300 K. Because the diffuse scattering intensity originates from the displacement of bridging halide ions, this result indicates that approximately 30% of the chains afford no diffuse scattering at 300 K.

The STM technique is a powerful tool for investigating local valence structure, and an STM measurement was performed on the present compound in order to clarify the local electronic state. Figure 11 shows an STM image of  $[\text{Pt}(\text{chxn})_2\text{I}]_2$  on the  $bc$  plane recorded at room temperature. Within the area enclosed with white lines in Fig. 11, the bright spots indicating  $\text{Pt}^{\text{IV}}$  sites were observed approximately every 11 Å along the chain. Because the Pt-Pt distance along the chain is actually *ca.* 5.5 Å, these spots reflect the two-fold periodicity of the sample. The bright spots are distributed along the  $c$ -axis with a spacing of approximately 7 Å, with a correlation of 5 or 6 sites observed. This indicates that the

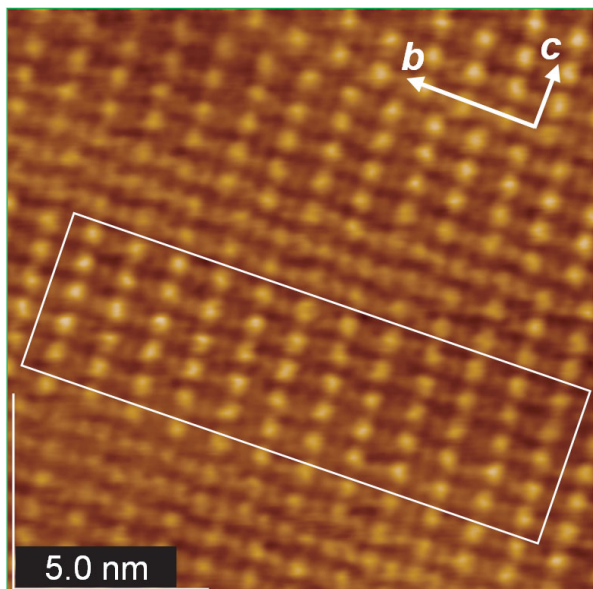


Figure 11  
STM image of  $[\text{Pt}(\text{chxn})_2]_2$  at room temperature. The region enclosed by the white rectangle indicates the area in which the CDW phase is aligned with the same phase.

CDW phase has a short-range ordering of phase along the  $c$ -axis, a finding consistent with the X-ray diffuse scattering results. It is noteworthy that in the boundary region at which the CDW phase inverts, the bright spots are observed every approximately  $5.5 \text{ \AA}$  along the chain. This area represents about 30% of the total area, in good agreement with the observed decrease in the X-ray diffuse scattering intensity.

From these findings, we are led to two possibilities for the electronic state at the CDW phase boundary. One possibility is the formation of a *static*  $-\text{Pt}^{\text{III}}-\text{I}-\text{Pt}^{\text{III}}-\text{I}-\text{Pt}^{\text{III}}-$  averaged-valence state. In this state, no diffuse scattering should be observed because the bridging iodide ions are located at the midpoint between neighboring Pt ions. The other possibility is a *dynamic* fluctuation between  $\text{Pt}^{\text{II}}$  and  $\text{Pt}^{\text{IV}}$  states. In this situation, the CDW correlation along the chain should be broken, resulting in broadening out of diffuse scattering peaks. Furthermore, if the fluctuation rate is much faster than the STM timescale, the presence of this state should lead to an STM image similar to that for a  $-\text{Pt}^{\text{III}}-\text{I}-\text{Pt}^{\text{III}}-\text{I}-\text{Pt}^{\text{III}}-$  averaged-valence state.

In order to obtain information on thermally excited states, we recorded X-band ESR spectra, which is sensitive on an intermediate timescale. We succeeded in observing a broad spectrum ( $340 \pm 50 \text{ G}$ ) at  $5 \text{ K}$ , which is attributable to signal due to static  $\text{Pt}^{3+}$  species. In contrast, a sharp spectrum ( $160 \pm 20 \text{ G}$ ) was observed at  $290 \text{ K}$ . By analyzing these spectra, we can assume that a para-magnetic species is hopping with the rate of  $2 \times 10^9 \text{ Hz}$  at  $290 \text{ K}$ , a rate which is slower than the X-ray timescale, but faster than the STM timescale. Therefore, we can conclude that the valence fluctuation is thermally activated at the boundary region of the CDW phase in  $[\text{Pt}(\text{chxn})_2]_2$ .

S. Takaishi<sup>1, 2</sup>, D. Kawakami<sup>1</sup>, M. Yamashita<sup>1, 2</sup>, Y. Wakabayashi<sup>3</sup>, H. Sawa<sup>3</sup>, H. Tanaka<sup>4</sup> and S. Kuroda<sup>4</sup> (<sup>1</sup>Tohoku Univ., <sup>2</sup>JST-CREST, <sup>3</sup>KEK-PF, <sup>4</sup>Nagoya Univ.)

## References

- [1] S. Takaishi, D. Kawakami, M. Yamashita, M. Sasaki, T. Kajiwara, H. Miyasaka, K. Sugiura, Y. Wakabayashi, H. Sawa, H. Matsuzaki, H. Kishida, H. Okamoto, H. Watanabe, H. Tanaka, K. Marumoto, H. Ito and S. Kuroda, *J. Am. Chem. Soc.*, **128** (2006) 6420.

## 2-6 *In-situ* Time-Resolved Dispersive XAFS Study on a Pt/C Cathode Catalyst in a Fuel Cell

Fuel cells have the potential to solve environmental and energy problems in modern society, but the activity and life time of Pt/C cathode catalysts must be improved to make fuel-cell automobiles a reality. Power-on and power-off processes (rapid voltage changes in the fuel cell) with high energy transfer are indispensable for commercial applications of fuel-cell systems. However, surface atoms of the active Pt particles tend to dissolve slightly into the electrolyte that is in contact with the cathode catalyst layer, and undesired Pt particles (or layers) deposit in the electrolyte. This is a serious problem because automobiles, in particular, require continual repetition of the on/off processes with rapid changes in cell voltages to alter the car's speed.

In order to overcome these problems, reaction mechanisms of the dynamic events on the electrode surfaces must be investigated *in situ* during voltage-stepping processes in real time. We have studied the electrochemical reaction mechanism at a Pt/C cathode surface in a fuel cell in rapid voltage-controlled processes by *in-situ* time-resolved dispersive XAFS (DXAFS) at the PF-AR NW2A station and found a significant time lag between electron transfer processes and redox structural changes of a Pt-cathode catalyst for the first time [1].

DXAFS measurements at Pt  $L_{\text{III}}$ -edge were conducted using the experimental setup shown in Fig. 12(a). A XAFS cell was prepared for the *in-situ* measurement of fuel-cell catalysts (anode: Pd/C, cathode: Pt/C).  $\text{H}_2$  and  $\text{N}_2/\text{air}$  gases were bubbled through deionized water baths before entering each electrode of the XAFS cell and reacted at the MEA (Membrane Electrode Assembly) as shown in Fig. 12(a). Si(111) was used as a polychromator and energy-dispersed X-rays were detected by a position sensitive detector of a photodiode array. A potentiostat for recording electrochemical data was synchronized to the position sensitive detector (PDA), and DXAFS spectra were recorded every 4 ms.

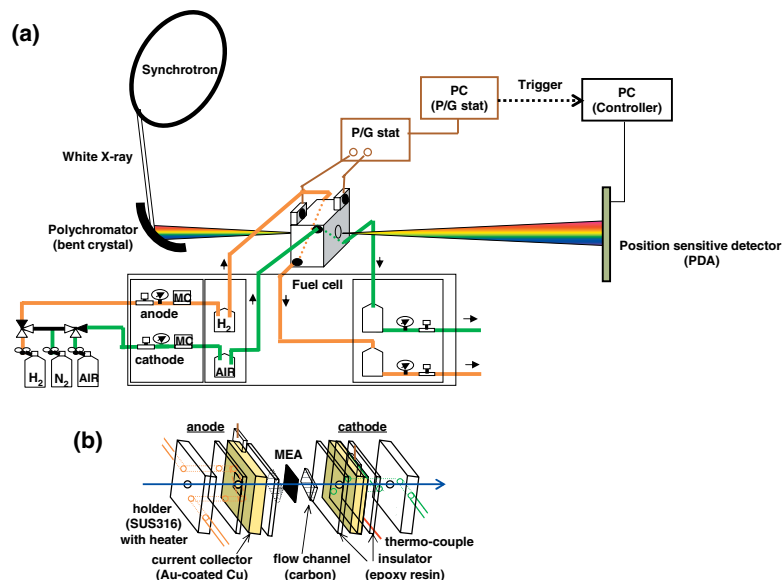


Figure 12  
 (a) DXAFS set-up for the *in-situ* measurements of fuel-cell catalysts and (b) the arrangement of a prepared *in-situ* XAFS cell for measurement in transmission mode.

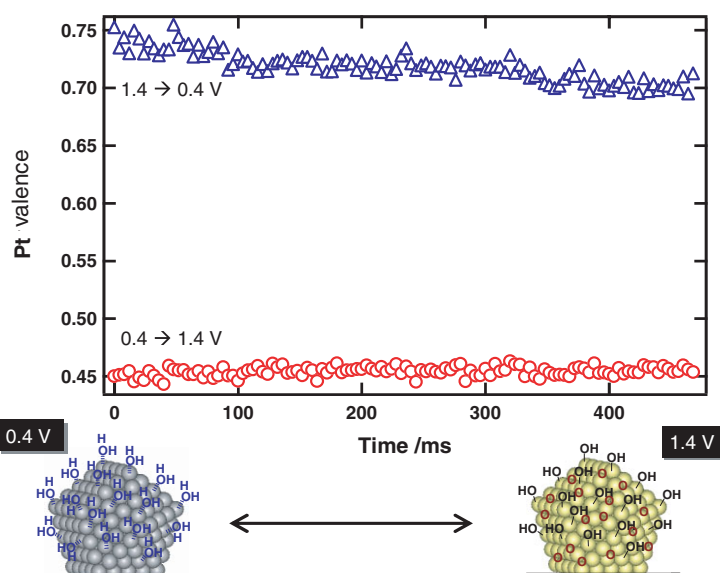


Figure 13  
 Changes in Pt valences of the Pt/C cathode catalyst measured by Pt  $L_{3}$ -edge DXANES at 4-ms time resolution. Red plots (○) represent the changes in Pt valence estimated by peak areas of DXANES in the voltage-operating process from 0.4 V to 1.4 V under  $N_2$ . Blue plots (△) represent the changes in Pt valence in the process from 1.4 V to 0.4 V.

When the cell voltage was stepped from 0.4 V to 1.4 V, electron transfers rapidly proceeded and the rate constants of the two electrochemical reactions monitored by potentiostat were estimated to be  $0.40 \text{ s}^{-1}$  and  $0.040 \text{ s}^{-1}$ . On the other hand, the Pt catalyst at the cathode surface slowly charged and the white line intensity of Pt  $L_{III}$ -edge DXANES was almost constant within the initial 500 ms as shown in Fig. 13. These results indicate that there was a significant time lag between the electron transfer reactions in the fuel cell and the structural changes of the Pt catalyst at the cathode.

A similar time lag between electron transfer and Pt discharging was also observed at a reverse voltage-operating process from 1.4 V to 0.4 V. The reaction rate of Pt discharging (1.4  $\rightarrow$  0.4 V) was faster than that of Pt charging (0.4  $\rightarrow$  1.4 V) as shown in Fig. 13, but the

Pt discharging took 2 min and was much slower than the electron transfer reactions. The first operando DXAFS measurements of a Pt/C cathode catalyst under the working conditions revealed the unique mechanism of the electrochemical reactions at the cathode surface of a fuel cell for the first time [1].

**M. Tada<sup>1</sup>, S. Murata<sup>2</sup>, T. Asaoka<sup>3</sup>, K. Hiroshima<sup>3</sup>, Y. Uemura<sup>1</sup>, Y. Inada<sup>4</sup>, M. Nomura<sup>4</sup> and Y. Iwasawa<sup>1</sup>**  
 (<sup>1</sup>The Univ. of Tokyo, <sup>2</sup>Toyota Motor Corp., <sup>3</sup>Toyota Central R&D Labs. Inc., <sup>4</sup>KEK-PF)

#### Reference

- [1] M. Tada, S. Murata, T. Asaoka, K. Hiroshima, K. Okumura, H. Tanida, T. Uruga, H. Nakanishi, S. Matsumoto, Y. Inada, M. Nomura and Y. Iwasawa, *Angew. Chem. Int. Ed.*, **46** (2007) 4310.